Optics & Laser Technology 192 (2025) 113879

Contents lists available at ScienceDirect

Optics and Laser Technology

journal homepage: www.elsevier.com/locate/optlastec

Full length article

Time-resolved analysis of carbon monoxide emissions from vehicles using a quartz-enhanced photoacoustic sensor

Mariagrazia Olivieri [a], Andrea Zifarelli [a], Angelo Sampaolo [a,b], Vincenzo Spagnolo [a,b], Pietro Patimisco [a,b,*]

[a] PolySense Lab, Dipartimento Interateneo di Fisica M. Merlin, Università degli Studi di Bari Aldo Moro e Politecnico di Bari, Via G. Amendola 173, Bari 70125, Italy
[b] PolySense Innovations srl, Via Amendola 173, Bari 70126, Italy

ARTICLE INFO

Keywords:
Vehicle atmospheric pollution
CO emissions monitoring
Real-time and fast exhaust detection
Gas sensing technology

ABSTRACT

Low-cost sensors networks hold the promise of dense spatial mapping over wide areas, through a combination of its price point and transportability, with a fine spatial reconstruction of the pollutants. Their reliability and the limited performance, particularly at finer temporal resolutions, represents the other side of coin. These shortcomings in dynamic environments pose serious challenges for their use in exposure studies and mobile applications. A recommendation for careful calibration, strategic experimental design, and an emphasis on high temporal resolution use cases are essential for guiding future technological development without losing key features, such as portability and compactness. In this work, we used a Quartz-Enhanced Photoacoustic Spectroscopy (QEPAS)-based sensor for sequentially measuring carbon monoxide (CO), nitrous oxide (N_2O), and water vapor emissions near vehicle exhaust pipes. With detection limits of 150 ppb for N_2O and 91 ppb for CO, this sensor allows for precise emission measurements. Moreover, the 300 ms temporal resolution enables real-time tracking of emission variations with a detailed temporal analysis. Field tests at the University of Bari Campus parking area confirmed the sensor capability to capture CO concentration fluctuations from both idling and moving vehicles.

1. Introduction

Vehicle exhaust emissions are widely recognized as a significant source of air pollution, particularly in urban and industrial areas [1,2]. Vehicle emissions consist of various gases released into the atmosphere because of fuel combustion in engines. These gases include carbon dioxide (CO_2), a major contributor to global warming, carbon monoxide (CO), which is toxic to humans and a greenhouse gases precursor, nitrogen oxides (NO_x), which contribute to smog and acid rain, and hydrocarbons (HC), which can lead to ground-level ozone formation. Additionally, particulate matter (PM) from diesel engines poses serious health risks [3]. Among these pollutants, nitrous oxide (N_2O) is one of the least emitted gases, with concentration less than 10 % above its natural abundance (~0.3 ppm), yet it has a global warming potential approximately 300 times higher than CO_2 [4,5]. Vehicles emission standards have been established to control pollutants in many countries, and in Europe these regulations are defined by the Euro emission standards, which classify vehicles based on their emission levels. Introduced in 1992 with Euro 1, these standards have progressively become stricter, with the latest being Euro 6 for passenger cars and Euro 7 set to take effect in the coming years [6,7]. Compliance with these standards is essential for manufacturers to market vehicles in regulated regions. Additionally, to improve the efficacy of measurement, the latest European emission regulations have implemented the Real Driving Emissions (RDE) test, which measures vehicle emissions under real-world driving conditions using Portable Emission Measurement Systems (PEMSs) [8–11]. Unlike traditional laboratory tests, these measurements are performed with vehicles driven on public roads across a diverse range of conditions, ca0pturing real-time primary emissions of CO, NO_x, PM, and fine dust. The emissions measured during real-world driving are referred to as actual emissions. The most advanced and reliable PEMS currently utilize optical gas analysis methods, including non-dispersive infrared detection (NDIR) and chemiluminescence detection (CLD) [12,13]. Despite the response rapidity, these methods suffer low sensitivity. Moreover, the 1-minute temporal resolution of the employed equipment did not allow for accurately capturing variations in NO_x and CO

* Corresponding author.
E-mail address: pietro.patimisco@uniba.it (P. Patimisco).

https://doi.org/10.1016/j.optlastec.2025.113879
Received 30 May 2025; Received in revised form 23 August 2025; Accepted 4 September 2025
Available online 8 September 2025

concentrations released in the air. Recently, Horiba introduced a PEMS based on Tunable Diode Absorption Spectroscopy (TDAS) with a Herriott multipass cell, enhanced by a modulation approach to improve sensitivity, for sequential N_2O and NH_3 detection [14,15]. However, the primary limitation lies in the large volume of the Herriott multipass cell. Despite claims of real-time monitoring, the time required to fill the cell, combined with gas exchange delays, prevents a truly dynamic, temporal, analysis of emissions. Moreover, the detection limits reported as the 3σ-value of the noise level (0.2 ppm for N_2O and 0.15 ppm for NH_3) are well above the natural abundance of both gas species. Despite the advancements in technology, detecting transient emissions remains essential for gaining a deeper understanding of engine behavior, fuel combustion cycles, and the impact of external factors. A faster acquisition rate would enable the capture of short-lived emission peaks that would otherwise go undetected with lower-frequency sampling. In urban environments, vehicle emissions can momentarily surge during acceleration, idling, or gear shifts. Therefore, a new approach is required that combines high-temporal resolution measurements with high sensitivity and a minimal sampling volume. This combination could provide a powerful and novel tool for real-time air quality monitoring in urban and industrial areas, enabling the study of plume diffusion and its persistence in atmosphere, tracking the spatial and temporal evolution of gas concentrations beyond natural levels, detecting acute pollution events such as traffic surges, and facilitating correlation studies between emissions and vehicle engine activity.

While QEPAS has been extensively investigated for trace-gas detection, its implementation for monitoring transient vehicle exhaust emissions in open-air environments has not been previously demonstrated. Our study utilizes a quartz-enhanced photoacoustic spectroscopy (QEPAS) sensing system [16–22] as an alternative to conventional PEMSs to monitor air quality by sequentially detecting carbon monoxide, nitrous oxide, and water vapor near vehicle exhaust pipes. The QEPAS system encompasses a Quantum Cascade Laser (QCL) emitting at 4.6 μm as light source and an Acoustic Detection Module (ADM), housing a spectrophone composed of a quartz tuning fork (QTF) and a pair of millimeter-sized resonator tubes to probe the photoacoustic effect within the ADM [23]. With an ADM having an internal net volume of less than 10 cm^3 and a total gas line length of ~ 1 m with 6 mm diameter tubing, the system ensures low volumes and rapid gas exchange times, enabling real-time tracking of multiple gas species, switching among them. The QEPAS system was initially used to monitor indoor concentrations of the three gas species over three days before shifting focus to outdoor CO and N_2O emissions from cars. For this purpose, the system was mounted in an open parking area at the University of Bari Campus, where it tracked CO and N_2O diffusion in the atmosphere. Emissions were monitored by idling vehicles parked 20 cm far from the sensor station, as well as from moving cars passing nearby the QEPAS system. This approach distinguishes itself from conventional PEMS systems, which generally lack the temporal resolution or portability needed for such dynamic monitoring.

2. Material and methods

2.1. Quartz-enhanced photoacoustic spectroscopy sensor

The schematic of the QEPAS sensor system is shown in Fig. 1.

The light source was an AdTech QCL with a central emission wavelength of 4.61 μm. The QCL temperature was controlled and its driving current was supplied using a Thorlabs ITC4002QCL Combined Current Driver and Thermoelectric Cooler (TEC). The laser light was focused by means of a 75 mm focusing lens (L) and then spatially filtered by using a pinhole (P) before entering the ADM. The ADM was designed as a small, compact gas cell that houses a QEPAS spectrophone, with two windows for laser light entry and exit, and an inlet/outlet for gas flow. The gas detection principle is based on photoacoustic effect, consisting in detection of sound waves generated by non-radiative energy relaxation of optically excited molecules, caused by the absorption of infrared modulated light resonant with a selected optical transition. In QEPAS, the sensing element is a spectrophone, consisting of a QTF and a pair of resonator tubes positioned on either side of the QTF [24–27]. This arrangement allows the laser beam to pass through the tubes and be focused between the prongs of the QTF. Hence, due to photoacoustic effect, acoustic waves are generated between the QTF prongs. The acoustic waves deflect the two prongs in opposite directions, exciting the antisymmetric flexural vibration mode if the acoustic frequency matches the QTF resonance mode frequency or one of its subharmonics [28,29]. The strain field induced on the QTF prongs generates a polarization field due to the piezoelectric properties of quartz. The generated quadrupole charge distribution is efficiently collected by a proper design of the electrode layout, thus producing a detectable electrical signal. Instead, any acoustic source located outside the area between the prongs will excite symmetric modes that, due to the electrode layout, are not piezoelectrically active, thereby ensuring immunity to environmental noise [16]. Moreover, at atmospheric pressure, the full width al half

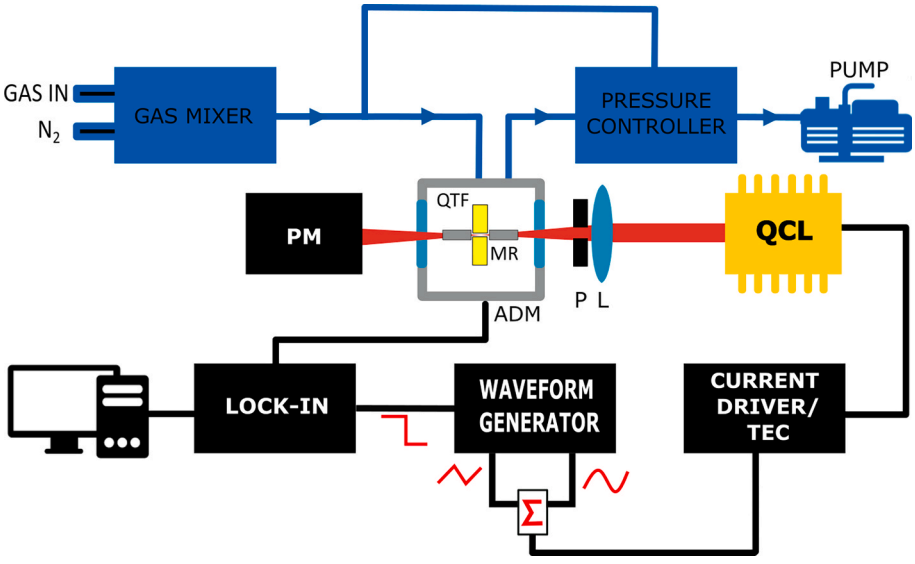

Fig. 1. Sketch of the employed experimental setup: QTF (quartz tuning fork), MR (micro-resonators tubes), ADM (acoustic detection module), QCL (quantum cascade laser), P (pinhole), L (lens).

maximum (FWHM) of the QTF resonance curve of the fundamental antisymmetric flexural mode is generally lower than 1 Hz [30]. This narrow bandwidth ensures highly efficient frequency selectivity, further reducing the impact of ambient noise on the QEPAS signal, making it ideal for environmental applications. A power meter (PM) was positioned behind the ADM for precise alignment. Additionally, the power meter continuously monitored laser power during both indoor and outdoor measurements at 1 Hz sampling rate, eventually enabling compensation for signal drift induced by power variations.

The QEPAS sensor system was operated in wavelength modulation and second harmonic detection [16]. A triangular ramp and a sinusoidal dither were applied to the laser source to finely tune the laser emission wavelength and modulate the laser light at the half of the QTF fundamental resonance mode $f_0/2$, respectively. The QTF piezoelectric current was converted into an electrical signal by a transimpedance amplifier (not shown in Fig. 1) and the f_0-component was extracted by a 5 MHz Zurich lock-in amplifier at an acquisition time of 300 ms.

The gas handling system includes an MCQ Instrument Gas Blender (GB-100) to manage flow rates and produce desired gas mixtures for both laboratory calibration or air sampling during outdoor measurements. For outdoor sampling operations, the inlet of the sensor system was equipped with a EU5 filter (compliant with the EN 779 standard) to prevent contamination of the ADM by dust and heavy pollutants. This filter provides high filtration efficiency (>99 %) for particles with a diameter greater than 1 μm. A laboratory test was conducted to confirm that the filter does not affect the composition of CO, N_2O, and water vapor in the sampled air (see Supplementary file). An ALICAT pressure controller/flow meter coupled with a pump allowed fixing the gas pressure and monitoring the flow rate inside the gas line. All measurements were conducted at fixed conditions of 300 Torr pressure and 50 sccm flow rate. The operating pressure value was chosen as the one that maximizes the QEPAS signal, resulting from the balance between the increase in molecular absorption and the decrease in QTF quality factor with varying pressure. Additionally, a hygrometer continuously monitored ambient relative humidity and temperature at 1-minute sampling rate, with these values subsequently converted into absolute humidity.

2.2. Laboratory calibration of the sensor system

As a first step, reference spectral scans were acquired with the QEPAS sensor system by directly sampling laboratory air through the gas mixer's input channel. The AdTech QCL operated at 15 °C, with a triangular ramp sweeping the QCL current from 238 mA to 308 mA at, resulting in a wavenumber range from 2188.7 to 2190.6 cm^{-1}, at a repetition rate of 5 mHz. The chosen spectral region allowed for the simultaneous detection of CO and N_2O absorption features, as well as water vapor, while the optical power varies between 23 mW and 43 mW during each scan. Fig. 2a presents a comparison between spectral scans of laboratory air (red line) and pure nitrogen (black line). These experimental results were compared to HITRAN simulation of absorption cross-section for an air sample at 300 Torr (1.19 % H_2O, 310 ppb N_2O, 150 ppb CO, and 77.87 % N_2 as rest) in Fig. 2b [31]. Fig. 2c reports the stick spectrum for each molecular species (N_2O, CO, and H_2O) in term of linestrength of each absorption line weighted by the analyte concentration. This provides a one-to-one association between the absorption features in Fig. 2b and the corresponding molecular species.

Within the selected spectral range, two N_2O absorption peaks were identified at 2189.27 cm^{-1} and 2190.34 cm^{-1}, with linestrengths of 7.67 $\times$ 10^{-26} and 8.64 $\times$ 10^{-26} cm/molecule, respectively. The other N_2O weak absorption features are expected to generate signals below the sensitivity of the QEPAS sensor. The absorption feature observed at 2190.02 cm^{-1} is attributed to a CO absorption line characterized by a linestrength of 4.31 $\times$ 10^{-26} cm/molecule, whereas the peak at 2189.43 cm^{-1} is associated to water vapor.

The sensor was then calibrated for N_2O and CO detection using two certified gas cylinders, one containing 10 ppm of N_2O and the other 8 ppm of CO, both in a nitrogen (N_2) matrix. By diluting them with a pure N_2 cylinder, analyte concentrations were varied in the range 2–10 ppm and 1–8 ppm for N_2O and CO, respectively. Sensor calibration was carried out through scanning the QCL current in the whole spectral range of Fig. 2a. The two N_2O absorption features located at 2189.27 cm^{-1} (P1) and 2190.34 cm^{-1} (P2) were efficiently reconstructed. The peak values were plotted as a function of the N_2O concentration in Fig. 3a.

It is worth noting that the difference in amplitude between the P1 and P2 signals can be attributed to the dependence of the QEPAS signal S

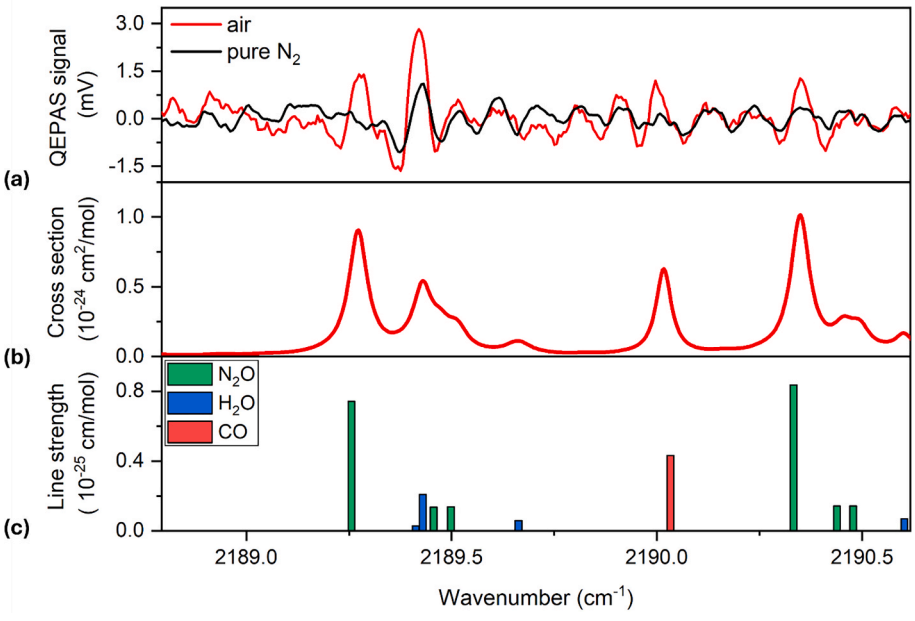

Fig. 2. (a) Spectral scans of laboratory air (red line) and pure nitrogen (black line). (b) HITRAN simulations of absorption cross-sections for an air sample at 300 Torr (1.19 % H_2O, 310 ppb N_2O, 150 ppb CO, and 77.87 % N_2). (c) Linestrength stick spectrum for each molecular species (N_2O, CO, and H_2O).

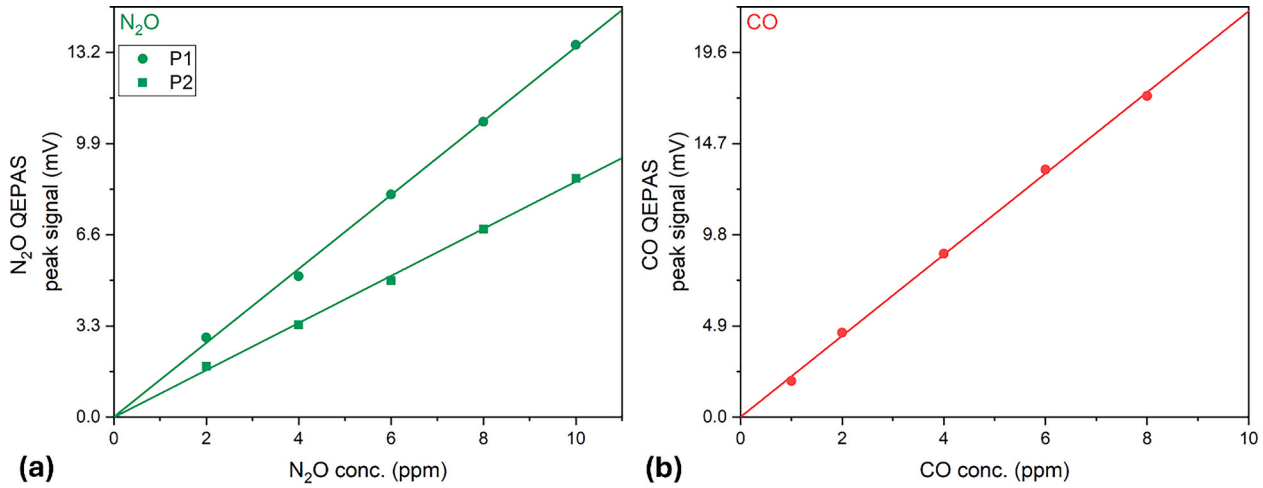

Fig. 3. QEPAS peak signals as a function of the gas target concentration for N_2O P1 (a, green circles), N_2O P2 (a, green squares) and CO (b, red circles). The solid lines represent the best linear fit.

on the laser power, following the relation $S \propto P\alpha Q$, where Q is the QTF quality factor, α the absorption coefficient, and P the laser power. As shown in Fig. 2a, moving toward lower wavenumbers corresponds to higher laser currents and, consequently, higher laser powers. Thus, the P1 peak is measured at a higher optical power than P2, leading to a larger QEPAS signal amplitude, despite its lower linestrength.

The best linear fit of the dataset provides the sensitivity of the QEPAS sensor system for N_2O detection, resulting $m_{N2O}^{P1} = 1.33$ mV/ppm and $m_{N2O}^{P2} = 0.85$ mV/ppm for P1 and P2, respectively. For both indoor and outdoor measurements, the N_2O concentration was determined by analyzing P2, as it provides the highest sensitivity.

The same procedure was applied during the calibration process for CO detection, where its peak values of the absorption feature at 2190.02 cm^{-1} (Fig. 2b) were analyzed as a function of CO concentration (Fig. 3b), yielding a sensitivity of $m_{CO} = 2.18$ mV/ppm. The three calibration curves report a negligible offset, meaning that the MDLs are not influenced by residual optical noise but are instead determined solely by the intrinsic thermal noise of the QTF.

The minimum detection limits (MDLs) were determined as the lowest analyte concentrations that produce a signal-to-noise ratio of 1. With a measured noise level of 0.2 mV (corresponding to the 1σ standard deviation of the QEPAS signal distribution in the absence of analytes in the ADM), the MDLs were calculated to be 150 ppb for N_2O and 91 ppb for CO.

2.3. Validation of the sensor platform

Validating sensors for environmental monitoring is essential to ensure their accuracy and reliability over time. Environmental conditions and contamination can impact sensor performance, leading to drift or altered responses that compromise measurement quality. For instance, gas sensors used in air quality monitoring can experience baseline shifts or changes in sensitivity, which may affect the detection of target gases. Regular calibration and performance checks are therefore important to maintain sensor accuracy and reliability, ensuring consistent, high-quality data for long-term environmental monitoring.

The accuracy of the QEPAS system can be primarily affected by two factors: degradation of the resonance properties of the spectrophone and changes in the sensitivity values established during the calibration process. Consequently, during both indoor and outdoor measurements, the acquisition was periodically paused to reconstruct both the spectrophone's resonance curve and the N_2O absorption features P1 and P2, in sequence. The latter was done by switching from air sampling to a gas line containing a cylinder of 10 ppm N_2O in N_2 upstream. As an example, the spectrophone resonance curves and the 10 ppm N_2O absorption features from indoor measurements run performed on January 9th are shown in Figs. 4a and 4b, respectively.

The spectrophone resonance curves were reconstructed in the excitation frequency range 12456–12465 Hz. A Lorentzian fit was superimposed on the experimental data to determine the resonance frequency (f) and FWHM of the curve, allowing the estimation of quality factor Q as f/FWHM. The extracted values are listed in Table 1.

Figs. 4b, P1 peak values were extracted and compared with the calibration curve in Fig. 3a. An average N_2O concentration of 10.16 ± 0.17 ppm was calculated, which matches the expected value based on the gas cylinder concentration.

Both validation procedures confirmed that no recalibration or online re-adjustment of any working parameters are necessary during a full day of measurements, proving the robustness of the sensor system.

3. Results

3.1. Indoor air quality assessment

Fig. 5 presents the sequential detection of N_2O, CO, and H_2O in laboratory air, monitored over three days, specifically on January 9th, 10th and 13th, 2025. The laboratory volume measures 10 m × 7 m with a height of 3 m, and features forced external ventilation on one side, with a typical occupancy of two to three people. The data were acquired at a sampling rate of one point per minute, corresponding to the time required for the sensor system to scan the entire laser current range and extract peak values associated with the three gas species. The bottom panel also displays the absolute humidity values measured at 1-minute sampling rate by an external hygrometer placed close to the sensor system.

In the absence of anthropogenic or natural sources of CO and N_2O in the laboratory, the average values closely match the expected natural abundance and remain consistent throughout the three days of measurement. The absolute humidity measured by the external hygrometer reveals how water vapor levels can vary from day to day, influenced by various unpredictable factors. This variation impacts the QEPAS H_2O signal, which reflects the water vapor in the gas line. Indeed, the sensor operates in a flowing regime, utilizing a gas handling system that includes a flow/pressure controller and a pump to draw humidified laboratory air into the ADM. As the flow passes through, water vapor can adhere to the internal walls just as easily as it can be released, due to the well-known adhesion effect of strong polar molecules like water vapor. Consequently, the gas mixture entering the ADM, and in turn the QEPAS H_2O signal, reflects only in part the humidification of sampled air, which

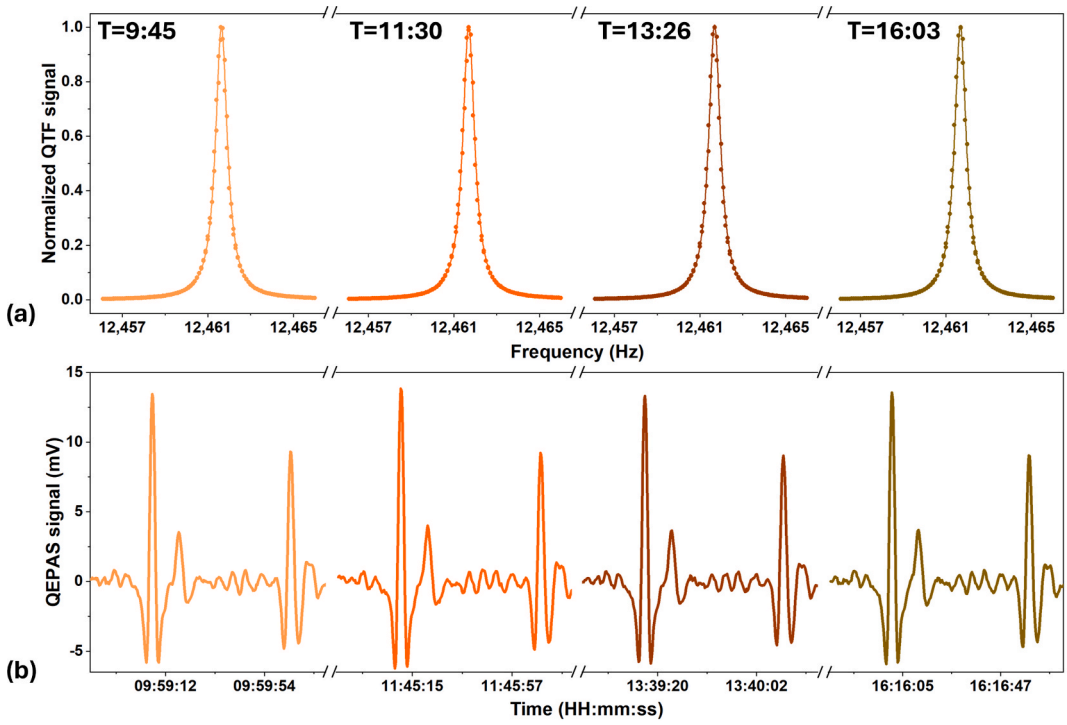

Fig. 4. (a) Frequency response of the spectrophone (quartz tuning fork coupled with resonator tubes) measured during indoor air quality assessment on January 9 at different recording times, during which air monitoring was temporarily interrupted. (b) QEPAS spectra measured immediately after each corresponding frequency response acquisition, using a 10 ppm N_2O certified gas mixture.

Table 1
Resonance frequency, FWHM and quality factor values calculated from the Lorentzian fit performed on the experimental data shown in Fig. 4 (top panel). The quality factor is calculated as the ratio of the resonance frequency to the FWHM. Uncertainties in the resonance frequency and FWHM are extracted from the Lorentzian fit, while the uncertainty in the quality factor is determined through error propagation.

Recording time (HH:mm)	9:45	11:30	13:26	16:03
f (Hz)	12461.635 ± 0.002	12461.692 ± 0.002	12461.684 ± 0.002	12461.683 ± 0.002
Δf (Hz)	0.671 ± 0.006	0.676 ± 0.006	0.671 ± 0.006	0.671 ± 0.006
Q	18572 ± 166	18434 ± 164	18572 ± 166	18572 ± 166

is expected to be influenced by external humidity.

3.2. Sequential outdoor detection of N_2O, CO, and H_2O

The sensor system was installed in the parking area of the Physics Department on the University of Bari Campus, strategically positioned near the traffic flow and adjacent to a parking spot. Fig. 6 presents a top-view of the parking area extracted from Google Maps.

The red dashed parking slot, located 20 cm from the sensor S, is designated for idling vehicles to allow continuous monitoring of N_2O and CO concentrations from vehicle exhaust gases. The arrows indicate the direction of vehicle movement: arrows labelled "A" represent the path of cars entering the parking area, while arrows labelled "B" indicates the path of cars exiting the parking area. Vehicles following the "A" flow pass approximately 50 cm away from the sensor at the closest position.

Fig. 7a reports the recorded concentrations of N_2O and CO on January 16th, between 10:40 AM and 03:50 PM along with the QEPAS H_2O signal and the absolute humidity measured by the hygrometer, with the same measurement approach used for the indoor monitoring. Since each scan takes 1 minute, the analyte concentrations are recorded at 1-minute intervals.

The shaded areas represent data collected when two different idling vehicles belonging to the same EURO4b class were parked near the sensor, within the red dashed parking slot of Fig. 6. During this period (from 11:00 to 11:45 AM), the CO concentration rose to ppm levels, compared to its natural abundance of approximately 350 ppb (Fig. 7b). Meanwhile, N_2O exhibited a slight 100 ppb increase, which is statistically insignificant as the variation falls within 3σ of the 150-ppb minimum detection limit, defined as the N_2O concentration yielding a signal-to-noise ratio (SNR) equal to 1. This outcome was expected, as Euro 4 and later vehicle classes are not considered relevant sources of N_2O, whose concentration typically remains close to its atmospheric background abundance. The small fluctuations observed confirm that the sensor response is consistent with the expected low emission profile. However, including N_2O in the detection scheme serves a dual purpose: first, it demonstrates the sensor's ability to sequentially monitor multiple gas species (CO, N_2O, and H_2O) with high sensitivity and rapid switching, validating the versatility of the compact QEPAS platform; second, it provides a benchmark for future applications where N_2O may represent a more significant emission component, such as in industrial or agricultural contexts in long-term outdoor campaigns.

From 12:00 AM to 03:50 PM, the red dashed parking slot was free from vehicles. During this time interval, over thirty vehicles passed through the sensor along the path marked by arrows A and B in Fig. 6, without causing a significant increase in CO levels. The data points in Fig. 7c corresponds to an average CO concentration of 350 ppb, with a standard deviation of 68 ppb, reflecting a pattern similar to that observed during the three days of indoor monitoring.

3.3. High-resolution CO detection from idling vehicles

To increase the acquisition rate, the laser current was locked on the CO peak. With a signal integration time of 0.1 s, the CO concentration

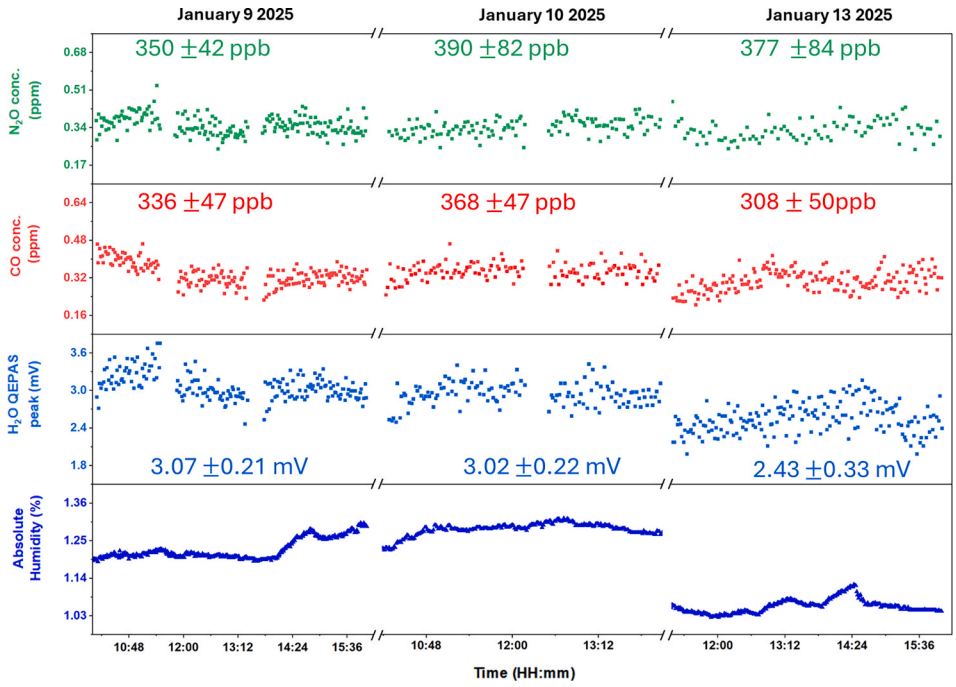

Fig. 5. Sequential detection of N_2O, CO, and H_2O in laboratory air (January 9, 10, and 13, 2025). The first and second graphs show N_2O and CO concentration variations over time, respectively, with the average values and 1σ-standard deviation values reported above each dataset. The third graph shows H_2O QEPAS signal variations over time, with the average values reported above each dataset. The fourth trend displays absolute humidity values recorded by an external hygrometer placed close to the QEPAS sensor system.

Fig. 6. Top-view of the parking area of the Physics Department on the University of Bari Campus extracted from Google Maps. The blue rectangle denotes the sensor location and the red dashed parking slot, located 20 cm from the sensor S, is designated for idling vehicles. The arrows (A e B) indicate the direction of vehicle movement.

was recorded every 0.3 s. Fig. 8a shows the CO monitoring data for two time periods: from 04:00 PM to 04:27 PM and from 04:30 PM to 04:52 PM on January 16th, with an idling EURO4b vehicle parked in the red-dashed parking spot.

The average CO emissions reach the ppm-level, and they display an oscillating pattern that is likely linked to the activity of the car's engine. These fluctuations in concentration suggest that the CO levels are closely tied to the engine's operation, with emissions increasing and decreasing in response to changes in engine load or speed. When the car is turned off, the CO concentration returns to its baseline level within 21 and 43 s during the two time periods, respectively, as shown in Figs. 8b and 8c. While the engine is running, an average CO concentration of 4.1 and 3.3 ppm is released into the atmosphere at 20 cm from the exhaust pipe of the vehicle.

3.4. Analysis of CO emissions from moving traffic

On January 17th, the sensor system was utilized in this configuration, for rapid, real-time CO detection tracking emissions from passing cars. Fig. 9 presents the CO concentration throughout the day at selected time intervals.

A video footage with a webcam enabled the synchronization of car passages with the timeline of Fig. 9 (Supplementary file). The green lines indicate the moments when a car enters the parking area, following the A arrows path in Fig. 6, while the blue lines mark when cars exit, following the B arrows path. The semi-transparent area represents the time interval during which an idling car remains parked near the sensor in the red dashed slot. When a car passes near the sensor, the CO release in the air shows a nearly instantaneous spike, followed by a rapid decline, as illustrated in the zoomed-in view in the three right panels (b), (c) and (d) of Fig. 9. Within less than 40 s, the CO level returns to its baseline and this explains why they were not detected when the sensor is in scanning mode (Fig. 7a). To measure CO emissions exclusively from moving traffic, we analyzed data collected in areas without idling vehicles parked near the sensor. The average CO concentration measured from 9:20 to 9:40 in the upper panel is 528 ppb. In the central panel the mean concentration measured from 12:45 to 13:58 is 460 ppb, while the one measured from 15:05 to 15:45 (lower panel) results 430 ppb. These measures are consistent with the daily averages (~600 ppb) collected the same day by the monitoring stations located in Via Caldarola (~1.6 km from the parking area) operated by the regional agency ARPA Puglia

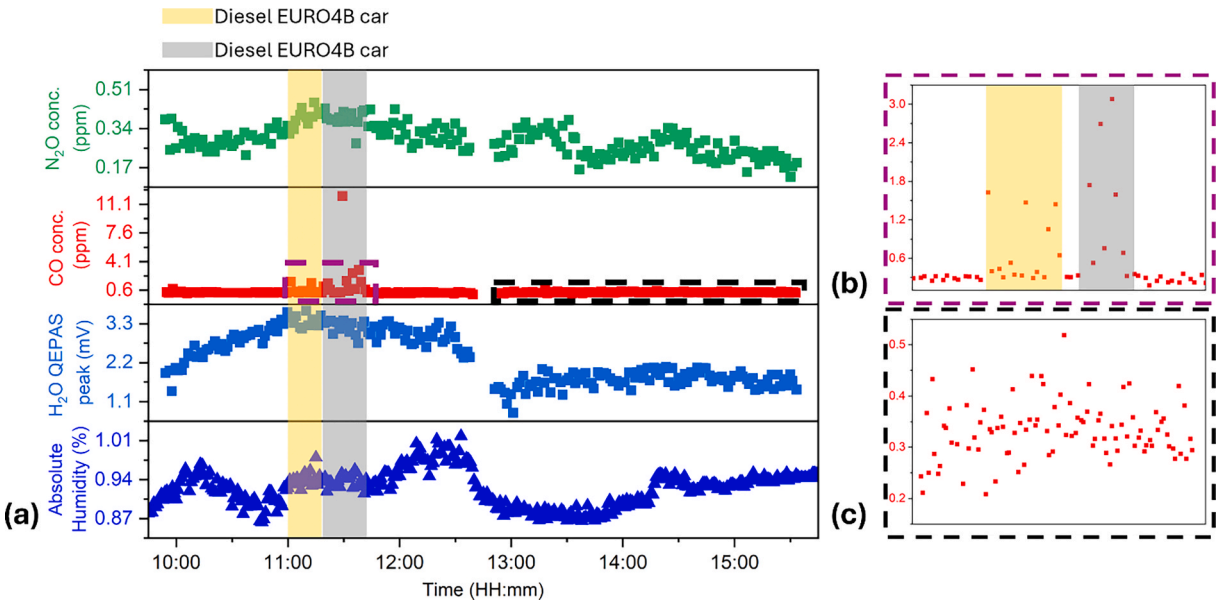

Fig. 7. (a) Sequential N_2O, CO, and H_2O detection in the parking area on January 16th. From top to bottom: the first and second panels show concentration variations of N_2O and CO, respectively. The third panel shows QEPAS signal for H_2O. The fourth panel displays absolute humidity values over time. The shaded areas represent data collected when two different idling vehicles (EURO4b class) were parked near the sensor. (b) Zoomed-in view of CO concentration data from 11:00 AM to 11:45 AM, highlighting fluctuations during the idling vehicle events. (c) Zoomed-in view of CO concentration data from 12:00 AM to 03:50 PM.

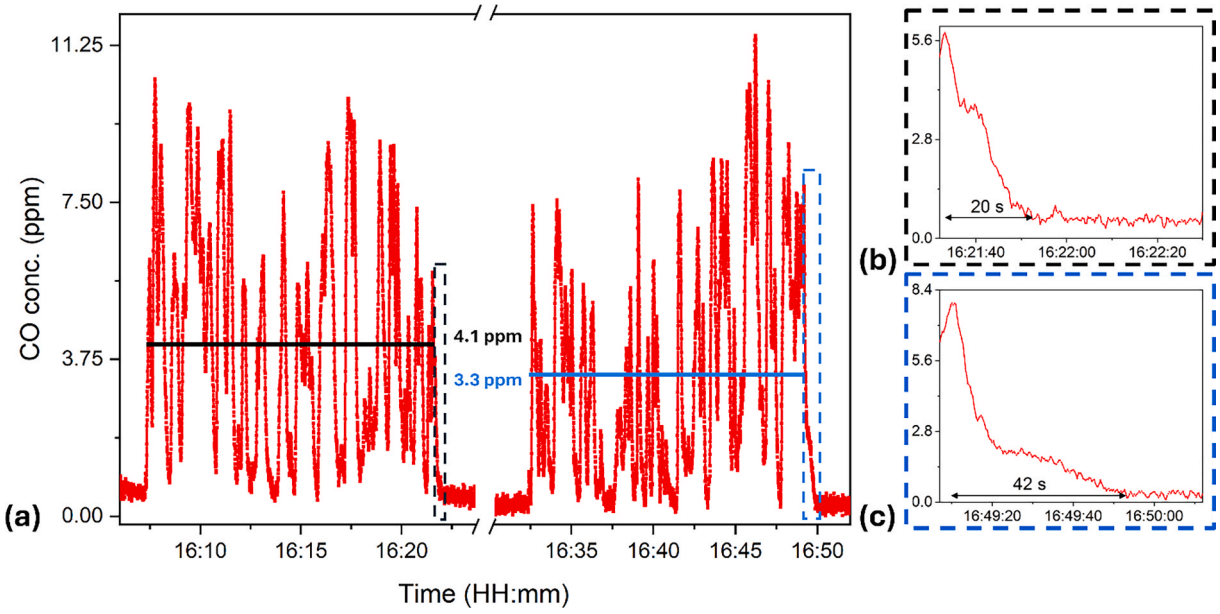

Fig. 8. (a) CO concentration variations over two-time windows with an idling EURO4b vehicle parked in the red-dashed parking spot shown in Fig. 6. The graph reports also the average CO concentrations as solid lines emitted from the exhaust pipe while the engine is running. (b) and (c) show a zoomed-in view of the CO concentration starting from the moment the engine was turned off, for each of the two-time windows.

[32]. Via Caldarola area is characterized by higher volume of traffic compared to the university parking area, which accounts for the slightly elevated average value measured.

4. Conclusions

In this work, we have demonstrated the application of a QEPAS-based sensor to real-time monitoring of transient vehicle exhaust emissions in open-air conditions. Unlike previous QEPAS implementations mainly targeting stable indoor environments or background monitoring, our system achieves sub-second resolution of CO emissions directly from idling and moving vehicles, thanks to its compact, low-volume design enabling rapid gas exchange. This represents a significant advance compared to conventional PEMS, which typically provide $\geq$ 1-minute resolution and are limited in capturing short-lived emission peaks. By enabling real-time detection and rapid response, we have demonstrated that our technology is fundamental for advancing sensing systems, ensuring efficient monitoring and management of atmospheric emissions. Critical challenges commonly associated with low-cost sensors have been effectively addressed, enhancing sensitivity, selectivity, and stability while also minimizing interference from environmental factors and sensor drift. While low-cost air sensors offer the advantage of high

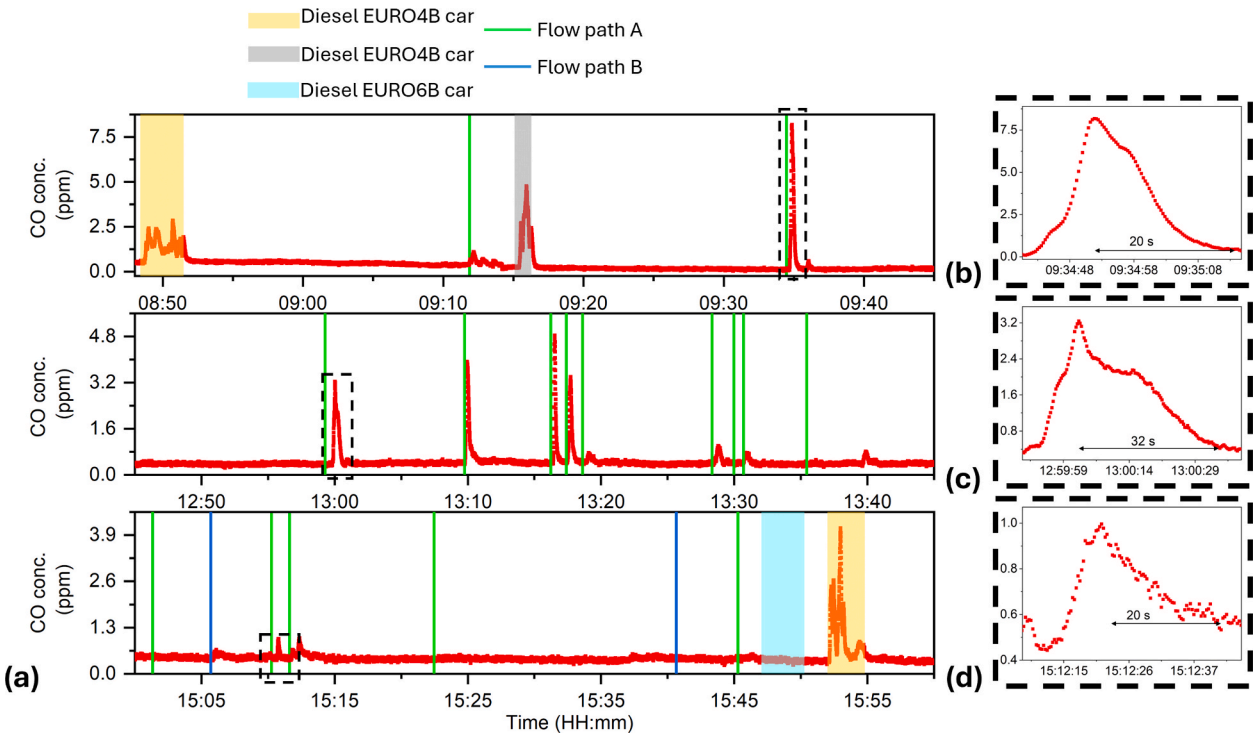

Fig. 9. CO concentration variation throughout the day (January 17th, 2025) during selected time windows. The green lines indicate the moments when a car enters the parking area, following the A arrows path in Fig. 6, while the blue lines mark when cars exit, following the B arrows path. The semi-transparent area represents the time interval during which an idling car remains parked near the sensor in the red dashed slot in Fig. 6. The three panels (b), (c) and (d) on the right provide a zoomed-in view of the time intervals highlighted by the black dashed box in panel (a). Each zoomed panel is aligned with the corresponding graph line from which it was extracted.

spatial density due to their affordability, they lack the capability to reconstruct temporal emission profiles accurately. Additionally, the delayed nature of validated data limits their potential for immediate analysis [33,34]. This presents a significant challenge for emerging trends that focus on integrating artificial intelligence (AI) into sensor networks for predictive analytics and autonomous decision-making [35–37]. Our sensor system achieves real-time monitoring of carbon monoxide (CO) emissions with sub-second resolution when the laser current is locked on the absorption peak of the target gas. In this configuration, the system can reconstruct the temporal dynamics of CO dispersion, as shown in Fig. 8a. By capturing the variations in CO emissions over time, it becomes possible to model how contaminants spread through the air, considering factors such as wind patterns, temperature fluctuations, and urban topology. Furthermore, our point-detection sensing system facilitates the study of the persistence of high-concentration gas puffs in the atmosphere. Indeed, Fig.s 8b, 8c and 9 prove that when the car was turned off or moved away from the sensor system, the CO emissions quickly returned to their baseline levels. This rapid decline highlights the direct influence of engine operation on CO concentration, demonstrating the capability of our system in detecting transient pollution events. This information is particularly valuable for algorithms designed for environmental monitoring and predictive modeling. AI-based models, such as machine learning and deep learning approaches, rely on high-resolution temporal data to improve their accuracy in forecasting pollution levels and identifying emission sources as well as to refine dispersion models, reducing uncertainties and improving decision-making processes [38,39]. By continuously learning from new data, these systems can adapt to changing environmental conditions.

Ultimately, our sensor system can be a powerful tool for rapidly verifying compliance with on-road emission standards. Its real-time detection capability allows for quick and efficient emission checks directly in real-world driving conditions, without the need for laboratory testing. Fig. 9a shows that when an idling Euro 6d vehicle is parked near the sensor system, no CO emissions are detected. This result aligns with expectations, as Euro 6d engines are designed for highly efficient combustion, precise air–fuel mixture control, and effective catalytic conversion, ensuring that any residual CO is fully oxidized into CO_2.

By providing immediate and accurate measurements, our sensor system can be deployed for roadside emission monitoring, enabling authorities and researchers to assess vehicle compliance in real traffic scenarios. This approach is particularly valuable for identifying high-emitting vehicles, validating regulatory standards, and supporting the development of smarter emission control strategies. Thanks to the intrinsic modularity of QEPAS, the system can be straightforwardly extended beyond CO and N_2O detection. Since the detection principle is wavelength-independent and does not require optical detectors, adapting the platform to other target species, such as NO_x and NH_3, only requires replacing the laser source while keeping the same sensor architecture. This flexibility has already been demonstrated in [40], where a single QEPAS configuration was employed to detect multiple pollutants by laser source switching. Moreover, the QEPAS sensor can be integrated with low-cost sensors for the simultaneous quantification of particulate matter (PM) [41]. Such a roadmap ensures the scalability of our platform to meet the upcoming Euro 7/RDE requirements while maintaining compactness, robustness, and cost-effectiveness.

CRediT authorship contribution statement

Mariagrazia Olivieri: Writing – review & editing, Writing – original draft, Visualization, Methodology, Investigation, Formal analysis, Data curation, Conceptualization. **Andrea Zifarelli:** Writing – review & editing, Visualization, Data curation, Conceptualization. **Angelo Sampaolo:** Writing – review & editing, Funding acquisition, Data curation, Conceptualization. **Vincenzo Spagnolo:** Writing – review & editing,

Funding acquisition, Data curation, Conceptualization. **Pietro Patimisco:** Writing – review & editing, Writing – original draft, Visualization, Methodology, Investigation, Funding acquisition, Formal analysis, Data curation, Conceptualization.

Declaration of competing interest

The authors declare that they have no known competing financial interests or personal relationships that could have appeared to influence the work reported in this paper.

Funding

The authors acknowledge financial support from the European Union's Horizon 2020 research and innovation program under grant agreement No. 101,016,956 PASSEPARTOUT, in the context of the Photonics Public–Private Partnership, PNRR MUR project PE0000023-NQSTI, project MUR – Dipartimenti di Eccellenza 2023–2027 – Quantum Sensing and Modelling for One-Health (QuaSiModO).

Appendix A. Supplementary data

Supplementary data to this article can be found online at https://doi.org/10.1016/j.optlastec.2025.113879.

Data availability

Data will be made available on request.

References

[1] K. Zhang, S. Batterman, Air pollution and health risks due to vehicle traffic, Sci. Total Environ. 450–451 (2013) 307–316, https://doi.org/10.1016/J.SCITOTENV.2013.01.074.
[2] J. Kagawa, Health effects of diesel exhaust emissions—a mixture of air pollutants of worldwide concern, Toxicology 181–182 (2002) 349–353, https://doi.org/10.1016/S0300-483X(02)00461-4.
[3] R. Westerholm, K.E. Egeback, Exhaust emissions from light- and heavy-duty vehicles: chemical composition, impact of exhaust after treatment, and fuel parameters, Environ. Health Perspect. 102 (1994) 13–23, https://doi.org/10.1289/EHP.94102S413.
[4] J.M. Dasch, Nitrous oxide emissions from vehicles, J. Air Waste Manag. Assoc. 42 (1992) 63–67, https://doi.org/10.1080/10473289.1992.10466971.
[5] K.H. Becker, J.C. Lörzer, R. Kurtenbach, P. Wiesen, T.E. Jensen, T.J. Wallington, Nitrous oxide (N2O) emissions from vehicles, Environ. Sci. Technol. 33 (1999) 4134–4139, https://doi.org/10.1021/ES9903330/ASSET/IMAGES/LARGE/ES9903330F00004.JPEG.
[6] Euro 1 to Euro 7 – Vehicle Emissions Standards | RAC Drive. https://www.rac.co.uk/drive/advice/emissions/euro-emissions-standards/.
[7] A. Zardini, P. Bonnel, Real Driving Emissions Regulation, 2020. https://doi.org/10.2760/176284.
[8] M. Kousoulidou, G. Fontaras, L. Ntziachristos, P. Bonnel, Z. Samaras, P. Dilara, Use of portable emissions measurement system (PEMS) for the development and validation of passenger car emission factors, Atmos. Environ. 64 (2013) 329–338, https://doi.org/10.1016/J.ATMOSENV.2012.09.062.
[9] L. Rubino, P. Bonnel, R. Hummel, A. Krasenbrink, U. Manfredi, G. De Santi, On-road emissions and fuel economy of light duty vehicles using PEMS: chase-testing experiment, SAE Int. J. Fuels Lubr. 1 (2008) 1454–1468, https://doi.org/10.4271/2008-01-1824.
[10] G. Fontaras, V. Franco, P. Dilara, G. Martini, U. Manfredi, Development and review of Euro 5 passenger car emission factors based on experimental results over various driving cycles, Sci. Total Environ. 468–469 (2014) 1034–1042, https://doi.org/10.1016/j.scitotenv.2013.09.043.
[11] M. Weiss, P. Bonnel, R. Hummel, U. Manfredi, R. Colombo, G. Lanappe, P. Le Lijour, M. Sculati, Analyzing on-road Emissions of Light-duty Vehicles with Portable Emission Measurement Systems (PEMS), 2011. https://publications.jrc.ec.europa.eu/repository/handle/JRC62639.
[12] Portable Emission Measurement PEMS / RDE. https://www.aip-automotive.de/en/Products/Emission-Technology/Portable-Emission-Measurement.
[13] PEMS Gasboard-9805. https://www.gas-analyzers.com/AutomobileExhaustGasAnalyzer.
[14] PEMS, Portable Emissions Measurement Systems | HORIBA Automotive. https://www.horiba.com/int/automotive/applications/emissions-performance-and-durability/exhaust-emissions/pems-testing/.
[15] Y. Kondo, S. Hamauchi, Y. Kowada, K. Shibuya, Y. Otsuki, Development of on-board multi-component gas analyzer toward euro 7, SAE Tech. Pap. (2023), https://doi.org/10.4271/2023-32-0026.
[16] P. Patimisco, A. Sampaolo, L. Dong, F.K. Tittel, V. Spagnolo, Recent advances in quartz enhanced photoacoustic sensing, Appl. Phys. Rev. 5 (2018) 011106, https://doi.org/10.1063/1.5013612.
[17] G. Menduni, A. Zifarelli, E. Kniazeva, S. Dello Russo, A.C. Ranieri, E. Ranieri, P. Patimisco, A. Sampaolo, M. Giglio, F. Manassero, E. Dinuccio, G. Provolo, H. Wu, D. Lei, V. Spagnolo, Measurement of methane, nitrous oxide and ammonia in atmosphere with a compact quartz-enhanced photoacoustic sensor, Sensors Actuators B. Chem. 375 (2023), https://doi.org/10.1016/j.snb.2022.132953.
[18] M. Olivieri, G. Menduni, M. Giglio, A. Sampaolo, P. Patimisco, H. Wu, L. Dong, V. Spagnolo, Characterization of H 2 S QEPAS detection in methane-based gas leaks dispersed into environment, Photoacoustics 29 (2023) 100438, https://doi.org/10.1016/j.pacs.2022.100438.
[19] S. Li, L. Dong, H. Wu, A. Sampaolo, P. Patimisco, V. Spagnolo, F.K. Tittel, Ppb-level quartz-enhanced photoacoustic detection of carbon monoxide exploiting a surface grooved tuning fork, Anal. Chem. 91 (2019) 5834–5840, https://doi.org/10.1021/acs.analchem.9b00182.
[20] Y.F. Wang, L.X. Liu, C.M. Gao, Z.Y. Lu, Y. Zhou, Review of quartz enhanced photoacoustic spectroscopy, J. Univ. Electron. Sci. Technol. China 44 (2015), https://doi.org/10.3969/j.issn.1001-0548.2015.06.025.
[21] R. Wang, S. Qiao, Y. He, Y. Ma, Highly sensitive laser spectroscopy sensing based on a novel four-prong quartz tuning fork, Opto-Electronic Adv. 8 (2025), https://doi.org/10.29026/OEA.2025.240275.
[22] S. Qiao, Y. He, H. Sun, P. Patimisco, A. Sampaolo, V. Spagnolo, Y. Ma, Ultra-highly sensitive dual gases detection based on photoacoustic spectroscopy by exploiting a long-wave, high-power, wide-tunable, single-longitudinal-mode solid-state laser, Light Sci. Appl. 13 (2024) 1–16, https://doi.org/10.1038/S41377-024-01459-5.
[23] Thorlabs - ADM01 Acoustic Detection Module for QEPAS, Hylok Fittings, BaF2 Windows. https://www.thorlabs.com/thorproduct.cfm?partnumber=ADM01.
[24] M. Olivieri, A. Zifarelli, G. Menduni, M. Di Gioia, C. Marzocca, V.M.N. Passaro, A. Sampaolo, M. Giglio, V. Spagnolo, P. Patimisco, Influence of air pressure on the resonance properties of a t-shaped quartz tuning fork coupled with resonator tubes, Appl. Sci. 11 (2021), https://doi.org/10.3390/app11177974.
[25] F.K. Tittel, D.V. Serebryakov, A.L. Malinovsky, I.V. Morozov, Applications of quartz tuning forks in spectroscopic gas sensing, Rev. Sci. Instrum. 27 (2002) 43105, https://doi.org/10.1364/OE.22.028222.
[26] A. Zifarelli, G. Menduni, M. Giglio, A. Elefante, A. Sukhinets, A. Sampaolo, P. Patimisco, S. Fangyuan, W. Chongwu, Q.J. Wang, V. Spagnolo, Compact and versatile QEPAS-based sensor box for simultaneous detection of methane and infrared absorber gas molecules in ambient air, front, Environ. Chem. 3 (2022) 1–11, https://doi.org/10.3389/fenvc.2022.926233.
[27] L. Dong, A.A. Kosterev, D. Thomazy, F.K. Tittel, QEPAS spectrophones: design, optimization, and performance, Appl. Phys. B 100 (2010) 627–635, https://doi.org/10.1007/s00340-010-4072-0.
[28] F.K. Tittel, A. Sampaolo, P. Patimisco, L. Dong, A. Geras, T. Starecki, V. Spagnolo, Analysis of overtone flexural modes operation in quartz-enhanced photoacoustic spectroscopy, Opt. Express 24 (6) (2016) A682–A692, https://doi.org/10.1364/OE.24.00A682.
[29] A. Elefante, M. Giglio, A. Sampaolo, G. Menduni, P. Patimisco, V.M. Passaro, H. Wu, H. Rossmadl, V. Mackowiak, A. Cable, F.K. Tittel, Dual-gas quartz-enhanced photoacoustic sensor for simultaneous detection of methane/nitrous oxide and water vapor, Anal. Chem. 91 (20) (2019) 12866–12873, https://doi.org/10.1021/acs.analchem.9b02709.
[30] A. Zifarelli, M. Giglio, G. Menduni, A. Sampaolo, P. Patimisco, V.M.N. Passaro, H. Wu, L. Dong, V. Spagnolo, S. Csutak, P. Patimisco, M. Giglio, A. Elefante, V.M. N. Passaro, F.K. Tittel, M. Deffenbaugh, V. Spagnolo, Partial least-squares regression as a tool to retrieve gas concentrations in mixtures detected using quartz-enhanced photoacoustic spectroscopy, Anal. Chem. 10926 (2019) 11035–11043, https://doi.org/10.1021/acs.analchem.0c00075.
[31] Hitran Database. https://hitran.org/.
[32] https://dati.arpa.puglia.it/qaria.
[33] F. Carotenuto, A. Bisignano, L. Brilli, G. Gualtieri, L. Giovannini, Low-cost air quality monitoring networks for long-term field campaigns: a review, Meteorol. Appl. 30 (2023) e2161, https://doi.org/10.1002/MET.2161.
[34] M.R. Giordano, C. Malings, S.N. Pandis, A.A. Presto, V.F. McNeill, D.M. Westervelt, M. Beekmann, R. Subramanian, From low-cost sensors to high-quality data: a summary of challenges and best practices for effectively calibrating low-cost particulate matter mass sensors, J. Aerosol Sci 158 (2021) 105833, https://doi.org/10.1016/J.JAEROSCI.2021.105833.
[35] S.M. Popescu, S. Mansoor, O.A. Wani, S.S. Kumar, V. Sharma, A. Sharma, V. M. Arya, M.B. Kirkham, D. Hou, N. Bolan, Y.S. Chung, Artificial intelligence and IoT driven technologies for environmental pollution monitoring and management, Front. Environ. Sci. 12 (2024) 1336088, https://doi.org/10.3389/FENVS.2024.1336088/PDF.
[36] S.L. Ullo, G.R. Sinha, Advances in smart environment monitoring systems using IoT and sensors, Sensors 20 (11) (2020) 3113, https://doi.org/10.3390/S20113113.
[37] C.T. Yang, H.W. Chen, E.J. Chang, E. Kristiani, K.L.P. Nguyen, J.S. Chang, Current advances and future challenges of AIoT applications in particulate matters (PM) monitoring and control, J. Hazard. Mater. 419 (2021) 126442, https://doi.org/10.1016/J.JHAZMAT.2021.126442.
[38] Q. Zhang, Y. Han, V.O.K. Li, J.C.K. Lam, Deep-AIR: a Hybrid CNN-LSTM framework for fine-grained air pollution estimation and forecast in metropolitan cities, IEEE Access 10 (2022) 55818–55841, https://doi.org/10.1109/ACCESS.2022.3174853.

[39] A. Alléon, G. Jauvion, B. Quennehen, D. Lissmyr, PlumeNet: Large-Scale Air Quality Forecasting Using A Convolutional LSTM Network, (2020). https://arxiv.org/abs/2006.09204v1.
[40] R. De Palo, A. Elefante, G. Biagi, F. Paciolla, R. Weih, V. Villada, A. Zifarelli, M. Giglio, A. Sampaolo, V. Spagnolo, P. Patimisco, Quartz-enhanced photoacoustic sensors for detection of eight air pollutants, Adv. Photonics Res. 4 (2023) 1–11, https://doi.org/10.1002/adpr.202200353.
[41] B. Alfano, L. Barretta, A. Del Giudice, S. De Vito, G. Di Francia, E. Esposito, F. Formisano, E. Massera, M.L. Miglietta, T. Polichetti, A review of low-cost particulate matter sensors from the developers' perspectives, Sensors 20 (23) (2020) 6819, https://doi.org/10.3390/S20236819.